The ageing effect in topological insulators: evolution of the surface electronic structure of

Bi_2Se_3 upon K adsorption

The ageing effect in topological insulators: evolution of the surface electronic structure of Bi_2Se_3 upon K adsorption

Kyungwha Park[1,3], Christophe De Beule[2] and Bart Partoens[2]

[1] Department of Physics, Virginia Tech, Blacksburg, VA 24061, USA
[2] Department of Physics, University of Antwerp, Groenenborgerlaan 171, B-2020 Antwerp, Belgium
E-mail: kyungwha@vt.edu

Abstract. Topological insulators (TIs) have attracted a lot of interest in recent years due to their topologically protected surface states, as well as exotic proximity-induced phenomena and device applications for TI heterostructures. Since the first experimental studies of TIs, angle-resolved photoemission spectra (ARPES) showed that the electronic structure of the topological surface states significantly changes as a function of time after cleavage. The origin and underlying mechanism of this *ageing effect* are still under debate, despite its importance. Here we investigate the evolution of the surface Dirac cone for Bi_2Se_3 films upon asymmetric potassium (K) adsorption, using density-functional theory and a tight-binding model. We find that the K adatoms induce short-ranged downward band bending within 2–3 nm from the surface, due to charge transfer from the adatoms to the TI. These findings are in contrast to earlier proposals in the literature, that propose a long-ranged downward band bending up to 15 nm from the surface. Furthermore, as the charge transfer increases, we find that a new Dirac cone, localized slightly deeper into the TI than the original one, appears at the K-adsorbed surface, originating from strong Rashba-split conduction-band states. Our results suggest possible

[3] Author to whom any correspondence should be addressed.

IOP Institute of Physics Φ DEUTSCHE PHYSIKALISCHE GESELLSCHAFT

reinterpretations of experiments because the new Dirac cone might have been observed in ARPES measurements instead of the original one that appears immediately after cleavage. Our findings are consistent with ARPES data and provide insight into building TI-heterostructure devices by varying the band-bending potential or film thickness.

S Online supplementary data available from stacks.iop.org/NJP/15/113031/mmedia

Contents

1. Introduction

Topological insulators (TIs) have attracted great attention due to topologically protected surface states [1–5] and possible applications in spintronics and thermoelectrics. Exotic phenomena such as the quantum anomalous Hall effect, the topological magneto-electric effect and the formation of Majorana modes, were proposed and explored for TIs interfaced with other types of materials [3–8]. The topologically protected surface states bridge the bulk band gap, induced by a band inversion due to strong spin–orbit coupling (SOC). Moreover, the surface states have a helical Dirac dispersion near the Fermi level which is crossed only an odd number of times between time reversal invariant k points [1–5]. Consequently, elastic backscattering is strongly suppressed at the surface, because spin-flip processes are forbidden as long as time-reversal symmetry is preserved. These properties were observed in angle-resolved photoemission spectra (ARPES) on Bi-based alloys and crystals [4, 5, 9, 10]. Among those materials, Bi_2Se_3 has been studied the most because it has a single Dirac cone at the surface, with the largest bulk band gap.

Since the first experimental studies of TIs, it was reported that the electronic structure of the topological surface states significantly changes as a function of time after cleavage [11–23]. It was observed that the Dirac point shifts to higher binding energies when time passes, indicating more electron-rich surfaces. Furthermore, Rashba-split states appear in the conduction band, together with M-shaped valence-band states. This *ageing effect* was explained as a consequence of band bending near the interface and different proposals were formulated in the literature for

the underlying mechanism. One explanation, motivated by the work of Urazdin *et al* [24], was an expansion of the van der Waals gap between the quintuple layers (QLs) of the structure after cleavage [25]. However, recent combined experimental and theoretical works [16, 17, 21, 22] showed that the ageing effect is similar to the effect of adsorption, based on experimental studies of controlled atomic and/or molecular adsorption on TIs. The resultant band bending was explained in terms of an electrostatic potential variation near the surface. In these studies, a weak potential that penetrates down to 10–15 QLs (10–15 nm) was needed to explain the experimental results. Surprisingly, so far, an explicit *ab initio* study of the ageing effect, using the adsorption of atoms or molecules on TIs, has not been made. A deeper understanding of the underlying mechanism behind the band bending should prove useful for the study of the effect of interfaces on the topological surface states in various proposed systems [3–8].

Here we present a theoretical study of the evolution of the surface Dirac cone for Bi_2Se_3 in the presence of asymmetric potassium (K) adsorption, using first-principles and tight-binding calculations. We have chosen K adsorption as a model system for general atomic and molecular adsorption, since a large charge transfer can be expected with K. In this way, small and large charge transfers to Bi_2Se_3 can be studied by varying the concentration or the distance to the surface of the K adatoms, accordingly. Furthermore, K adsorption on Bi_2Se_3 was experimentally realized [19, 22]. We simulate K atoms adsorbed on the *top* surface of thin Bi_2Se_3 films of one QLs using density-functional theory (DFT) including SOC, and study up to 20 QLs using a tight-binding model with an effective band-bending potential.

We show that the experimental findings, such as the appearance of strong Rashba-split conduction-band states and M-shaped valence-band states, can be explained by charge transfer due to K adsorption. Furthermore, our results show, in contrast to earlier proposals [16, 17, 21, 22], that the band bending affects only the top two to three QLs (2–3 nm), instead of 10–15 QLs (10–15 nm). Moreover, the binding energy of the top Dirac cone increases until it drops below the M-shaped valence-band states, while a new Dirac cone appears close to the top surface, developed from the Rashba-split conduction-band states. These results suggest possible reinterpretations of experiments, because the new Dirac cone might have been observed in ARPES measurements, instead of the original one.

To anticipate a little further, our results show that even for a two-QL slab, the topologically protected surface states at the bottom surface can be recovered by K adsorption at the top surface for high K concentration. Our findings suggest the possibility to engineer hybrid TI structures for desirable properties by tuning parameters such as adsorption layers and slab thickness.

2. Computational methods

We calculate the electronic structure for bulk Bi_2Se_3 and Bi_2Se_3 (111) slabs with K adatoms on the *top* surface using DFT including SOC self-consistently. We use the VASP code [26, 27] with the projector-augmented-wave method [28], within the generalized-gradient approximation [29]. We find that the bulk band gap is 0.28 eV, in agreement with experimental values of 0.3–0.35 eV [30]. The DFT calculations are limited to six QLs, because the hybridization between top and bottom surfaces is already very small for five QLs. This is clear from the hybridization gap at $\overline{\Gamma}$ for pristine slabs of five to six QLs, which is found to be of the order of meV, as shown in table 1 as a function of slab thickness. The optimal K position for one to three QLs with a given surface coverage Θ, is found by relaxing the topmost QL while keeping the other QLs fixed at the experimental value [31]. For slabs with four to six QLs, the

Table 1. Thickness dependence of the hybridization gap Δ at $\overline{\Gamma}$ for pristine Bi_2Se_3 slabs and the energy difference ΔE_d between the Dirac point localized at the top and bottom surface for fully K-adsorbed Bi_2Se_3 slabs ($\Theta = 1$). For three QLs, the value of ΔE_d is obtained using the midpoint of the apparent energy gap. The slight increase in ΔE_d for four QLs compared to five to six QLs, is related to the numerical accuracy.

# QLs	Δ (eV)	ΔE_d (eV)
1	0.857	N/A
2	0.111	0.315
3	0.036	0.609
4	0.013	0.704
5	0.006	0.678
6	0.003	0.672

optimized K position of the three-QL slab is used, because of the high computational cost. We find that the optimal vertical distance between the K adatoms and the slab is $2.17\,\text{Å}$ for all slabs, within the numerical accuracy. Compared to hcp, bridge, and on-top adsorption sites, we find that fcc adsorption sites are the most stable.

For thicker slabs, we rely on a tight-binding model. In this model, we consider up to third nearest-neighbor hopping between the s and p orbitals of Bi and Se, and include SOC as an on-site contribution. We use the lattice constants and tight-binding parameters from [32] which were obtained from fitting the bulk bands to DFT results. The hopping matrices are expressed using the method of Slater and Koster [33]. More computational details for both the DFT and tight-binding model can be found in the supporting information[4].

3. Results and discussion

The calculated band structures for K-adsorbed slabs of one to six QLs with a full surface coverage ($\Theta = 1$) are shown in figure 1. Results for lower surface coverage ($\Theta = 1/4$) are given in the supporting information (see footnote 4). First note that the double degeneracy present for pristine Bi_2Se_3 slabs is lifted due to broken inversion symmetry, except at the time reversal invariant points such as $\overline{\Gamma}$ and $\overline{M}$.

This section is further organized as follows. First, we discuss the identification of the surface states (section 3.1) and the overall features of the calculated band structures (section 3.2). Next, we investigate the effect of charge transfer between the K adsorption layer and the Bi_2Se_3 slab (section 3.3). Then we propose a band-bending mechanism (section 3.4) to explain the evolution of the surface and quantum-well (QW) states as a function of the amount of charge transfer (section 3.5). Finally, we compare our calculated results with reported ARPES data, and propose a possible reinterpretation of the experimental results (section 3.6).

---

[4] Supporting information available at stacks.iop.org/NJP/15/113031/mmedia: details of the tight-binding model, movies of the evolution of the electronic band structure of a 20-QL TI slab from the tight-binding calculations, the minimal model hamiltonian, as well as band structure and electron density plots for K-adsorbed two to four QLs with surface coverages of unity and a quarter, obtained from DFT calculations.
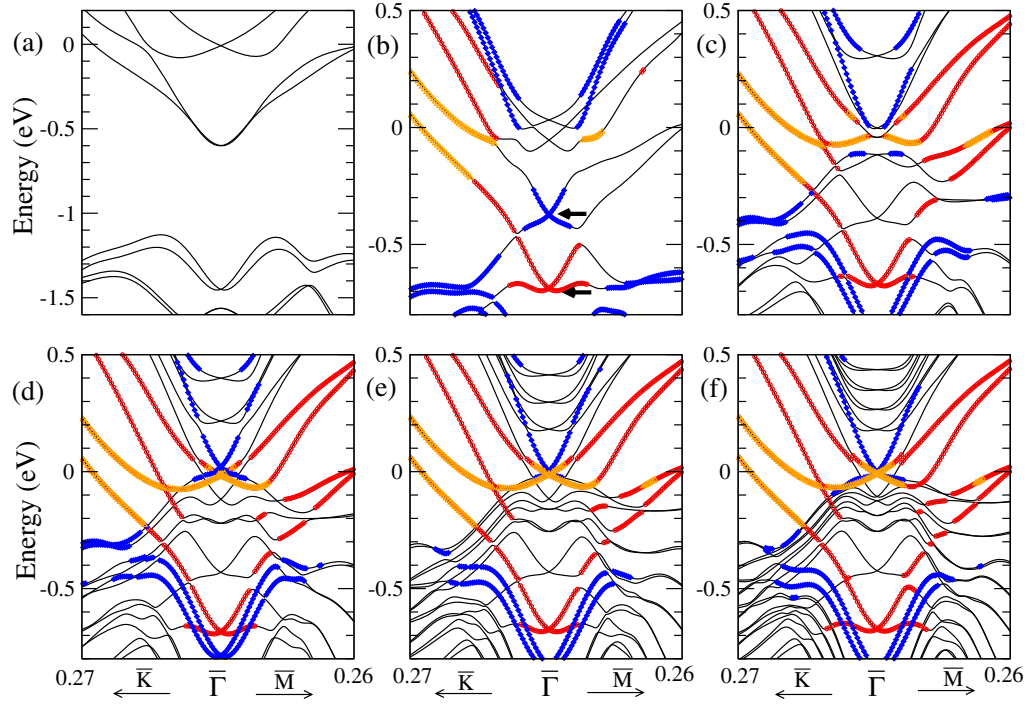
Figure 1. (a)–(f) Calculated band structures for fully K-adsorbed ($\Theta = 1$) Bi_2Se_3 slabs of one to six QLs, respectively. Note that the vertical scale in (a) differs from that in (b)–(f). The Fermi level is taken as the zero of energy. The arrows in (b) point out the gapless Dirac cone on the top and bottom surfaces for two QLs. In (b)–(f), the red circles (blue diamonds) indicate surface states at the top (bottom) surface, and the orange triangles indicate K-dominated states ($>30\%$ of the electron density from K), while the unmarked curves represent bulk-like states. Surface states are identified if more than 70, 60, 50, 40 or 40% of the electron density for the two, three, four, five and six QLs comes from the topmost or bottommost QL, respectively.

3.1. Identification of the surface states

The surface states are identified by projecting the electron densities on the individual atomic layers. In this way, we can clearly distinguish surface states from bulk-like states [34]. This is explicitly shown for the fully K-adsorbed five-QL slab in figures 2(c) and (d) for ten states at the $\overline{\Gamma}$ point. These states are labeled a1–a10, and are marked in the corresponding band structure, shown in figure 2(a). We proceed by discussing the characteristics of these states.

We assign states a4 and a10 as surface states from the bottom (bss) and top (tss) surfaces, respectively, because they are mostly localized in the bottommost and topmost QL, similarly to the surface states of the bare slab. State a5 clearly represents a K-dominated or impurity band very close to the Dirac point of the bottom surface. The states a1–a3 and a6–a9 in figures 2(a)–(d) are identified as bulk-like or QW states. Although the band crossings a6 and a9 show Dirac-like dispersion near $\overline{\Gamma}$, they are not true surface states because they are mostly localized in the second topmost QL.
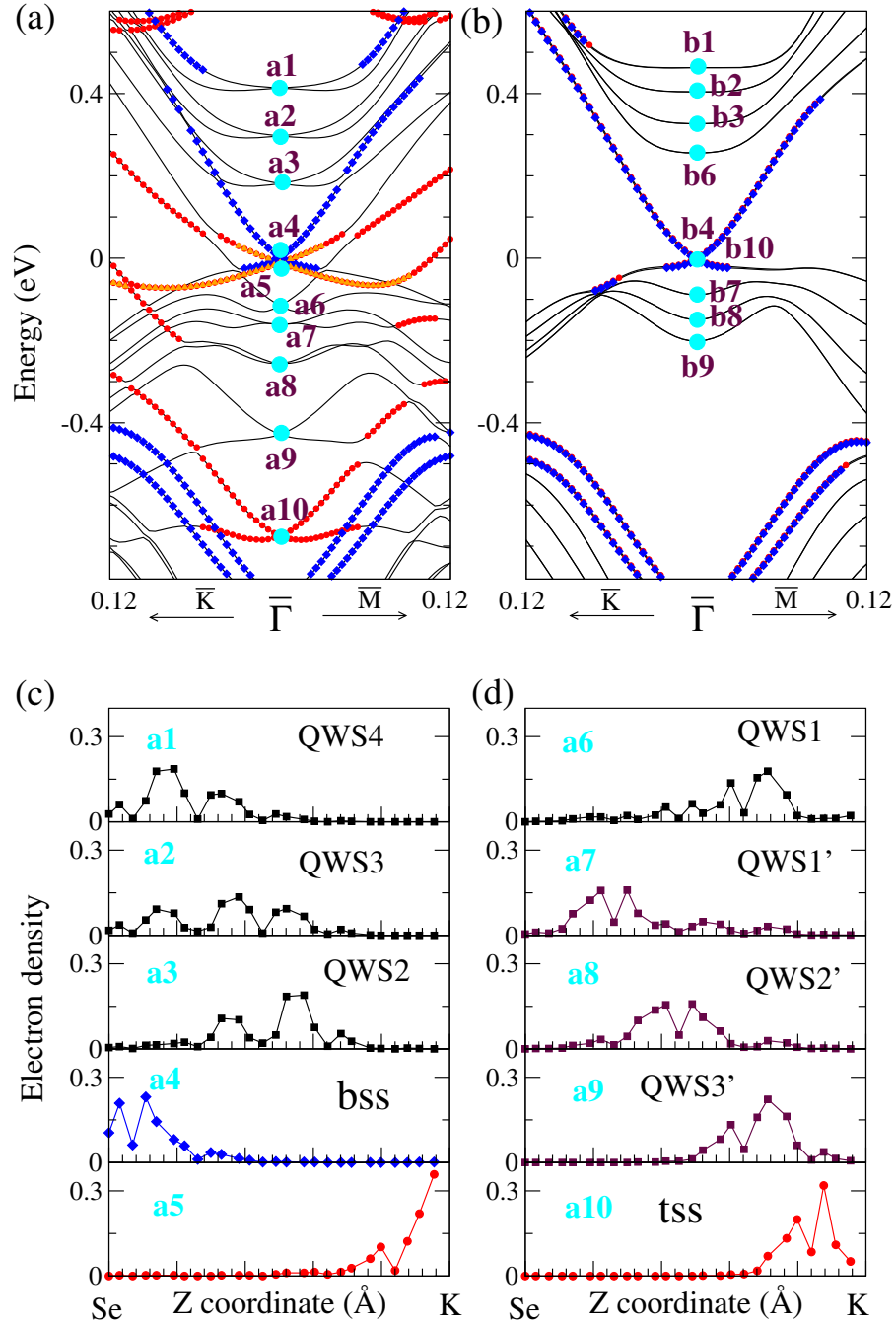
Figure 2. Band structure close to $\overline{\Gamma}$ for five QLs with a full K coverage (a) and the bare five-QL slab (b). (c)–(d) Layer-projected electron densities of the states a1–a10 at $\overline{\Gamma}$ as shown in (a). The color scheme in (a) is the same as that in figure 1.

The corresponding states for the pristine five-QL slab are labeled b1–b10 in figure 2(b). The same analysis has been made for two to six QLs upon K adsorption, for which the band structures are shown in figures 1(b)–(f). The projected electron densities are also shown for

fully K-adsorbed two to three QLs in figure S4 of the supporting information (available from stacks.iop.org/NJP/15/113031/mmedia).

3.2. Overall features of the band structure

Several observations can be made regarding the band structures shown in figure 1. First, we focus on the similar band structures for four, five and six QLs in figures 1(d)–(f). Interestingly, we find that the surface states at both top and bottom surfaces have a *gapless* Dirac dispersion near $\overline{\Gamma}$. The top-surface Dirac point is shifted downward relative to the bottom-surface Dirac point, showing an increased binding energy of about 0.7 eV. Note that the conduction-band QW states have a large Rashba spin-splitting, which was observed in ARPES measurements on Bi_2Se_3 with adsorption, surface impurities or aged bare Bi_2Se_3 [16–19]. It was also discussed in a DFT study of Bi_2Se_3 slabs with substitutional impurities [35].

For the thinnest system comprising one QL, a large band gap still persists (figure 1(a)). However, even for a very thin Bi_2Se_3 slab of two QLs with full K coverage, two distinct Dirac cones are present (figure 1(b)). This is in sharp contrast to a pristine two-QL slab where hybridization between both surfaces opens a gap. The gapless Dirac cones reappear because the cone that is localized at the top surface is shifted in energy because of the asymmetric K adsorption. This behavior can be explained by a minimal model for the surface states of a TI slab with structural inversion asymmetry [35, 36]. Additionally, note that the band gap of the two-QL slab (figure 1(b)) has increased to about 0.7 eV due to confinement. These results show a possibility of using confinement to increase the band gap, as requested for applications, while preserving the topologically protected surface states by separating them energetically.

Interestingly, for a fully K-adsorbed three-QL slab (figure 1(c)), the surface states at the top surface show a gapless Dirac dispersion, while the surface states at the bottom surface are not well defined at $\overline{\Gamma}$. In this case, strong coupling to bulk-like and K-dominated states causes an *apparent* energy gap of about 0.1 eV at $\overline{\Gamma}$ in the bottom-surface Dirac cone. However, the gap does not open at $\overline{\Gamma}$ itself and time-reversal symmetry is still preserved. The coupling strength can be adjusted by varying the coverage, slab thickness or the type of adsorption layer. Away from $\overline{\Gamma}$, the coupling reduces, which is shown in figures S4 and S5 of the supporting information.

3.3. Charge transfer: origin of local band bending

The origin of the local band bending is the charge transfer between the K-adsorbed layer and the Bi_2Se_3 slab, which leads to the creation of a surface dipole. The direction and the amount of charge transfer are obtained from comparing the layer-projected electron density $\rho(z)$ of a fully K-adsorbed Bi_2Se_3 slab, a bare Bi_2Se_3 slab and an isolated K layer, using the same unit cell, parameter values and k-point sampling. For this calculation, the geometries of the bare slab and isolated K layer are taken from the fully K-adsorbed slab. This is shown in figure 3(a) for a four-QL slab, as a function of the distance from the bottom surface z. Next, we calculate the electron density difference $\Delta\rho(z) = \rho(\text{adsorbed slab}) - \rho(\text{bare slab}) - \rho(\text{isolated K})$, as shown in figure 3(b). In order to find the total amount of charge transfer, we integrate $\Delta\rho(z)$ from the bottommost Se layer, to the midpoint between the topmost Se layer and the K adatom indicated as the vertical dashed line in figure 3. We find that 0.112 electrons per unit cell surface area (14.86 Å^2) or 0.0075 $e\,\text{Å}^{-2}$ are transferred from the K adatoms to the four-QL slab. For two
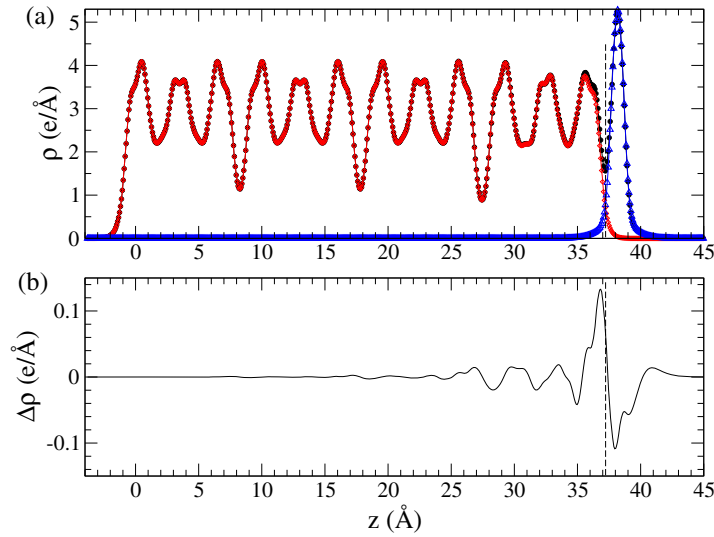
Figure 3. (a) Layer-projected electron densities of a four-QL slab with a full K coverage (black circles), the bare four QLs (red diamonds), and an isolated K layer (blue empty triangles), as a function of the vertical distance from the bottom surface z. (b) The electron-density difference $\Delta\rho(z)$ versus z. The vertical dashed lines in (a) and (b) denote the midpoint between the topmost Se layer and the K adatoms.

and three QLs, we find that 0.113 and 0.112 electrons per unit cell area are transferred to the slab. The amount of charge transfer does not change with slab thickness for a given K coverage within the numerical uncertainty. This is because the transfer occurs mostly within the topmost two to three QLs, as shown in figure 3(b).

A simple calculation shows that such a small charge transfer can indeed shift the binding energy of the top-surface Dirac cone about 0.7 eV downwards in energy. In bare Bi_2Se_3, the Dirac point is located close to the top of the bulk valence band, as shown in figure 2(b), and the conduction band starts at about 0.3 eV above it. If the Dirac cone is filled with electrons, starting from the Dirac point up to 0.3 eV, we can accommodate 0.01 electrons per unit cell surface area. For this calculation, we use the group velocity of the surface states close to $\overline{\Gamma}$ which is about 5.0×10^5 m s^{-1} [4, 5]. Going up to 0.7 eV, 0.06 electrons per unit cell surface area are needed to fill the cone. This is still smaller than the calculated charge transfer of the order of 0.1 electrons per unit cell surface area. However, while the top-surface Dirac cone has moved downwards, conduction-band states were also pulled down. Some of the conduction-band states fall below the Fermi level and become populated with a small fraction of electrons. This shows that a small charge transfer can indeed lead to a strong increase of the binding energy of the top-surface Dirac point, and an occupation of conduction-band states.

3.4. Band-bending mechanism

Based on the above results, we propose our band-bending scheme. In figure 4(a), we show the band diagram for a semiconductor–metal junction (Schottky barrier) before charge transfer, where the metal is given here by the adsorbed K layer. Note that the chemical potential of
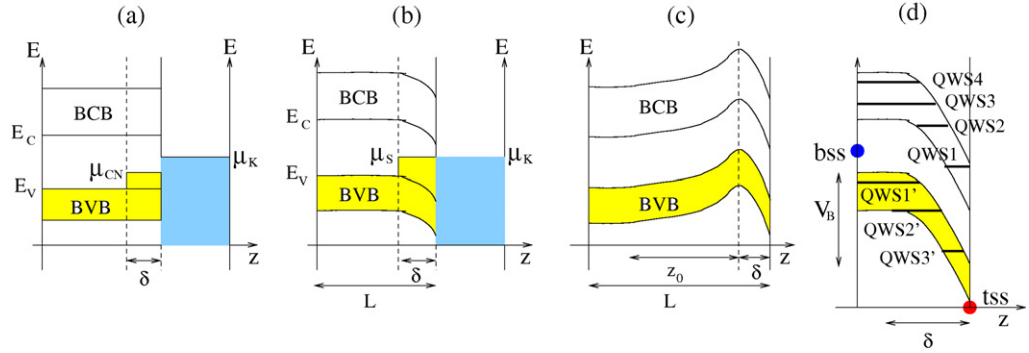
Figure 4. Schematic band diagrams of the semiconductor–metal junction (a) before and (b) after charge transfer. Here the metal is given by the adsorbed K layer. The chemical potential or charge neutrality point of the semiconductor, the K layer, and the surface, are given by μ_{CN}, μ_K and μ_S, respectively. The charge-transfer range is given by δ and L is the system size. (c) The combination of the upward band bending caused by the n-type doping with a wide depletion region of depth z_0, and the downward band bending due to the K layer over a narrow charge-transfer region of depth δ. (d) Band diagram of the downward band-bending region with the QW states and the bottom (blue) and top (red) surface Dirac points for a five-QL slab with a full K coverage.

the K layer μ_K is not necessarily aligned with the surface chemical potential μ_S or the charge neutrality point μ_{CN} of the slab. Indeed, the calculated work function for a free-standing K layer equals 2.39 eV, while the work function for a bare four-QL slab is 5.56 eV. In our case, this means that μ_K is well above the bulk conduction band of the slab.

If $\mu_K > \mu_S$, electrons from the K layer are transferred to vacant surface states of the slab. After the charge transfer, a dipole layer is formed at the interface and μ_K is aligned with μ_S, as illustrated in figure 4(b). The dipole points toward the bottom surface and is strongly localized at the interface within the topmost two to three QLs denoted by δ in figure 4. This result is consistent with the observation that the energy difference ΔE_d between the Dirac points of the bottom and top surfaces does not depend on slab thickness for slabs thicker than three QLs (see table 1).

Experimentally, it has been known that Bi_2Se_3 is naturally n-type doped. In the Schottky model, electron doping in semiconductors leads to *upward* band bending at the surface, as the surface states become occupied. This creates a depletion region into the bulk, with a characteristic depth z_0 of several tens of nanometers. On the other hand, as shown in figure 4(b), the charge transfer from the K adatoms to the surface leads to *downward* band bending in a charge region near the surface of depth δ, which is only a few nanometers wide. The combination of these two effects is illustrated in figure 4(c). In the Schottky model, this short-ranged downward band bending is ignored because $z_0 \gg \delta$ for typical semiconductors. In the proposed band-bending schemes from [16, 17, 21, 22], the downward band-bending region is much wider up to 15 nm. Therefore, we conclude that these schemes are not relevant to explain the ageing effect of Bi_2Se_3 slabs.

Figure 4(d) shows the final situation for the fully K-adsorbed five-QL slab. The small downward band-bending region leads to the formation of strongly localized QW levels as

demonstrated by the layer-projected electron densities in figures 2(c) and (d). In this case, the lowest-energy conduction-band state (QWS1) has a lower energy than the bottom-surface Dirac point (bss) due to the strong downward band bending. Interestingly, the top-surface Dirac point (tss) appears below the lowest-energy valence-band level QWS3'. Notice that in all previous studies [16–18, 21], it was always assumed that the top-surface Dirac point lies higher in energy than the valence-band QW states, originating from a much shallower band bending but penetrating much deeper than our scheme. Moreover, in ARPES experiments, another unidentified surface state was found below the the valence-band QW states [17, 18]. We suggest that this surface state is the original Dirac point of the top surface. As pointed out in the next section, the hybridization with valence-band QW states causes the top-surface Dirac cone to become less localized at the surface, making it harder to track with a surface technique such as ARPES.

Lastly, we discuss the effect of the downward band-bending in the thinner slabs of one to three QLs, whose band structures are shown in figures 1(a)–(c), respectively. The persistence of a band gap for one QL, is understood from the fact that the slab is so thin that the charge transfer affects both surfaces equally enough, still resulting in strong overlap between them. For two to three QLs, the binding energy of the bottom-surface Dirac cone increases by around 0.4 and 0.1 eV, respectively. This result is consistent with the extent of charge transfer and the band-bending depth. For the three-QL slab, the slab thickness is comparable to the size of the charge-transfer region, which explains the hybridization between the bottom surface state and QWS1, discussed earlier.

3.5. Ageing effect: evolution of surface and quantum-well states as a function of charge transfer

The motivation to study K adsorption is partly based on the large charge transfer that is expected for K. A smaller charge transfer can be realized by increasing the distance of the K atoms to the surface. This also simulates the experimental ageing effect, where the number of adsorbed atoms, and thus the amount of charge transfer, increases over a time scale of hours. Therefore, by examining the evolution of the electronic band structure near $\overline{\Gamma}$ as a function of the vertical distance between the K layer and the slab, we can investigate the ageing effect. We verified that results obtained in this way are similar to those for lower K concentrations, realized by taking a larger supercell. More details on this subject are included in the supporting information (available from stacks.iop.org/NJP/15/113031/mmedia) (see footnote 4). Due to the high computational cost, we present only the result for the K-adsorbed four QLs using DFT, and we use a tight-binding model with an effective band-bending potential for thicker slabs.

First we discuss the DFT calculations for the four-QL slabs. We consider an optimized K-adsorbed slab, a bare slab and slabs with K adatoms positioned at 4, 6 and 10 Å above the top surface, giving different amounts of charge transfer. In these calculations, we use the experimental lattice constants, i.e. we do not relax the structure, except for the optimized slab. We find that 0.087, 0.054 and 0.025 electrons per unit cell surface area are transferred to the slab for K adatoms at 4, 6 and 10 Å above the surface, respectively. For the optimized K-adsorbed slab, we find a charge transfer of 0.112 electrons per unit cell surface area. Here we use the same procedure to find the charge transfer as in section 3.3.

Figure 5(a) shows the evolution of the energies of the top-surface Dirac point and QW states relative to the bottom-surface Dirac point, as a function of the amount of charge transfer
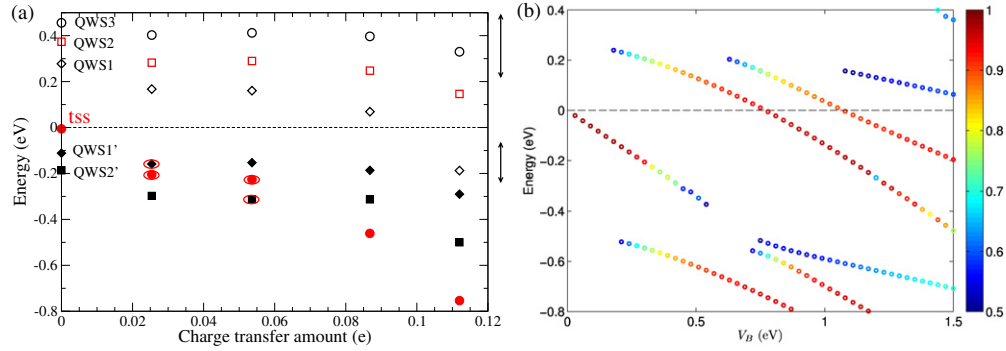
Figure 5. (a) Evolution of the top-surface Dirac point (red dots) and QW states at $\overline{\Gamma}$ as a function of the amount of charge transfer for the four-QL slab, calculated using DFT. The top surface state (tss) is identified as the state of which more than 50% is localized in the topmost QL. The encircled states in the second and third column, represent coupling between the tss and the corresponding QW states. The energy of the bottom-surface Dirac point (bss) is chosen as the zero of energy in all cases but the optimized slab. In the latter case, the binding energy of the bss increases slightly (about 0.05 eV). For the thicker optimized slabs such as five or six QLs, the bss is the same as that of the bare slabs. The width of the conduction and valence bands, calculated from a projection of the bulk bands, are given by the vertical arrows on the right. (b) Evolution of the energy levels at $\overline{\Gamma}$, projected on the top three QLs, as a function of V_B, obtained from tight-binding calculations for a 20-QL slab. This projection can be compared with the experimental ARPES data [17, 22] discussed in section 3.6. The color bar gives the percentage of density within the top three QLs.

for the four-QL slab. The different columns, from left to right, represent the energies of states for the bare slab, the slabs with K at 10, 6 and 4 Å above the surface, and the optimized K-adsorbed slab (K at 2.17 Å above the surface). As the charge transfer increases, the top-surface Dirac point moves downward faster than the energies of the QW states, so that it can hybridize with the valence-bands QW states. At a distance of 10 Å, the top-surface Dirac cone couples to QWS1', while at 6 Å, it couples to QWS2'. Upon further increasing the charge transfer, the top-surface Dirac point moves below QWS2' and becomes well separated from the valence-band QW states. Also note from figure 5(a) that QWS1, originating from the bulk conduction band, lies below the bottom-surface Dirac point for the maximum charge transfer.

The major features obtained from our DFT calculations shown in figure 5(a) are also supported by the tight-binding calculations where we include the effect of the charge transfer with an effective band-bending potential $V = -V_B\, e^{-z/w}$. Here V_B is proportional to the amount of charge transfer and w determines the charge-transfer range. Based on the DFT results, we have chosen $w = 1.5\,\mathrm{nm}$, resulting in a charge transfer range δ of approximately 3 nm (three QLs). This potential is given in figure S2 of the supporting information (available from stacks.iop.org/NJP/15/113031/mmedia). We can simulate the effect of the increasing charge transfer on the band structure by increasing V_B. The evolution of the bands near $\overline{\Gamma}$ for V_B from 0 to 1.5 eV is shown for a 20-QL slab in movie 1 of the supplementary information (see footnote 4). As V_B increases, the binding energy of the top-surface Dirac cone increases,

and hybridizes with some QW states originating from the valence band. At the same time, the lowest-energy Rashba-split conduction-band state (QWS1), moves downwards and transforms into a topological Dirac cone. In this case, it is not obvious anymore that the top-surface Dirac cone moves below all valence states upon large charge transfer, as was the case for the thin slabs. Now also valence band states are pulled downwards due to the charge transfer.

We also investigate the band bending for a deeper but weaker potential with the tight-binding model, as proposed in the literature. The best fit of the band-bending profile in figure 1(c) of [17] to the effective potential, is obtained for $w = 8$ nm. The evolution of the band structure for V_B from 0 to 0.5 eV is shown in movie 3 of the supplementary information (available from stacks.iop.org/NJP/15/113031/mmedia). Now there is no mixing between the top-surface Dirac cone and the valence-band states, and the Rashba splitting of the conduction-band states is very weak. Additionally, the lowest-energy conduction-band states do not form a second Dirac cone as V_B increases. This is also clear from the evolution at $\overline{\Gamma}$, which is shown in figure S3 of the supporting information. These observations are not in agreement with experimental results [16–19].

### 3.6. Comparison to experimental angle-resolved photoemission spectra data

Finally, we compare our results with ARPES measurements [17, 19] on Bi_2Se_3 with non-magnetic adsorption. ARPES is a surface technique, and therefore we project the electron density onto the top three QLs for the K-adsorbed slabs thicker than three QLs. In this section, we first discuss our DFT results for slabs of four to six QLs (figure 6) and then those of the tight-binding model for the 20-QL slab (figure 5(b)).

Figures 6(a)–(c) shows the projection for the K-adsorbed four QLs with K positioned at 10, 6, and 44 Å above the surface, respectively. Figures 6(d)–(f) shows the projection for the optimized K-adsorbed four, five and six QLs, respectively. Strong Rashba-split states are found in the conduction band, and M-shaped bands are clearly seen in the valence band, in accordance with experiments. From figures 6(a)–(d), we see that the lowest-energy level in the conduction band goes down in energy as the charge transfer increases. This state evolves further into an apparent Dirac dispersion near -5.7 eV in figures 6(d)–(f). It is instructive to compare figure 6(f) to the bands projected onto the *bottom* three QLs for the optimized K-adsorbed six-QL slab shown in figure 6(g), where the bottom-surface Dirac point is around -5.6 eV. These results suggest that the Dirac cone observed in experiments might not be the original top-surface Dirac cone, but a new Dirac cone, evolved from the Rashba-split conduction-band state QWS1.

For four and five QLs, the Dirac dispersion is gapless, while for six QLs there is an *apparent* energy gap in the projected band structure shown in figure 6(f). This gap is seen more clearly in figure 6(i) where we plot the projected band structure together with the original band structure, close to the bottom-surface Dirac cone. The entire band structure of the optimized K-adsorbed six-QL slab is shown in figure 7(a), together with the layer-projected densities in figures 7(b) and (c). The gap between states c5 and c6 in figures 6(i) and 7(a) appears due to coupling between the QWS1 and QWS1' at $\overline{\Gamma}$. This coupling causes the states c5 and c6 to become delocalized over the slab at $\overline{\Gamma}$ (figure 7(b)). Away from $\overline{\Gamma}$ the coupling is reduced, as shown by the projected electron densities for states d1 and d2 in figure 7(c).

We demonstrate that the short-ranged band bending explains most of the important features observed in the ARPES experiments [17, 19]. For example, the situation in figure 6(c) corresponds to figure 1(c) of [17]. The situation presented in figure 6(d) was not reached in
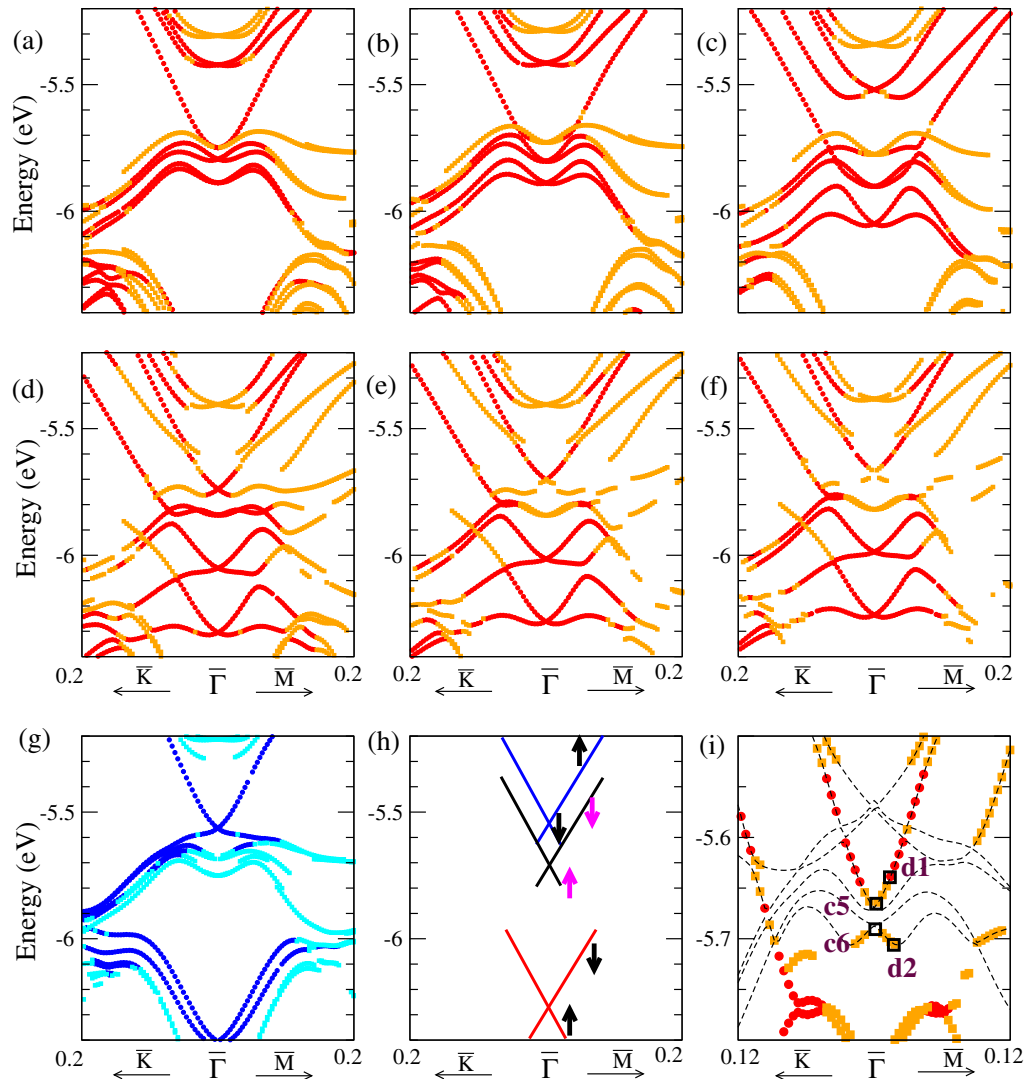
Figure 6. DFT-calculated projection of the bands on the top three QLs for (a)–(c) the four-QL slab with the K positioned at 10, 6, and 4 Å above the surface, and (d)–(f) the optimized fully K-adsorbed four, five and six QLs. The vacuum level is chosen as the zero of energy. To minimize the effect of periodicity, bands with significant K contributions with more than 30% are removed. (g) Projection of the bands on the *bottom* three QLs for the optimized K-adsorbed six QLs. (h) Schematic diagram of the spin structure for the bottom-surface Dirac cone (blue), the new Dirac cone (black), and the original top-surface Dirac cone (red), for the K-adsorbed slabs. (i) Zoom-in of (f) close to the apparent energy gap. The dashed curves are the bands before projection. The labeled states c5, c6, d1, and d2 are also shown in figure 7(a). The color scheme for (a)–(g), and (i) is as follows: red states have 90% or more of their density localized in the top three QLs, orange states between 65 and 90% in the top three QLs, blue states 90% or more in the bottom three QLs and cyan states between 65 and 90% in the bottom three QLs.
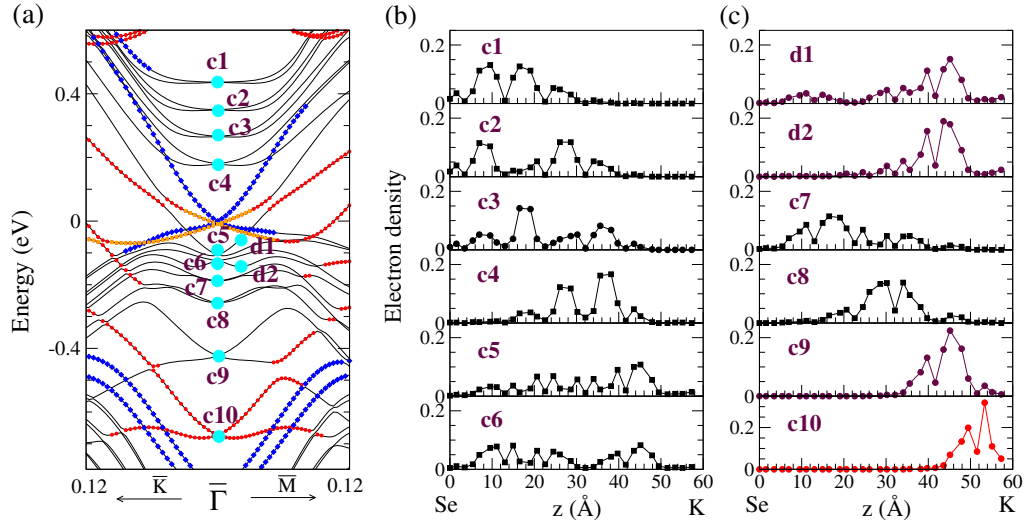
Figure 7. (a) Band structure of figure 1(f) close to the $\overline{\Gamma}$ point, and (b)–(c) the layer-projected electron densities, for the fully K-adsorbed six QLs. The color scheme in (a) is the same as that in figure 1.

this experimental study. This correspondence is also supported by our tight-binding model calculations for the 20-QL slab. In movie 2 of the supplementary information (available from stacks.iop.org/NJP/15/113031/mmedia) (see footnote 4), the same band structure evolution as in movie 1 is shown, but now projected on the top three QLs. As the potential depth V_B increases, the top-surface Dirac cone hybridizes with the M-shaped valence-band states, and the lowest Rashba-split states move downward while becoming increasingly more localized in the top three QLs. When the Rashba-split states reach the top of the valence band, they give rise to a new topological Dirac cone. From the DFT results, we find that the new Dirac cone does not have strict surface-state characteristics because the electron density is mostly localized in the second QL from the top, instead of the topmost QL. However, the spin structure of the new Dirac cone is similar to that of the original top-surface Dirac cone which is opposite to the spin structure of the bottom-surface Dirac cone, corresponding to the scheme shown in figure 6(h).

Several ARPES experiments measured the evolution of the energy states at $\overline{\Gamma}$ as a function of time after cleavage. Examples are figure 1 in [17] and figure 8 in [22]. We plot the same evolution as a function of the band bending depth V_B for the 20-QL slab in figure 5(b). Only states of which 50% or more are localized in the top three QLs are shown. The hybridization between the top-surface Dirac cone and the valence-band QW levels is clearly visible. Similar features can be recognized in the experimental data mentioned above.

4. Conclusion

We examined the evolution of surface states of Bi_2Se_3 films with asymmetric K adsorption as a function of film thickness and the amount of charge transfer, using DFT and a tight-binding model, in order to investigate the experimentally observed *ageing* effect. The asymmetric K adsorption creates well-separated top and bottom surface states with gapless Dirac dispersion even for a very thin slab of two QLs, as a consequence of charge transfer from the K adsorption

layer to the Bi_2Se_3 slab. Based on our calculations, we showed that the band-bending potential caused by the charge transfer has an unusually short range of 2–3 nm, in contrast to earlier proposals in the literature. Applying this short-ranged band-bending potential, we found that, as charge transfer increases, the top-surface Dirac cone moves downward in energy and can be strongly coupled to QW states. In addition, we were able to show the experimental observations of strongly Rashba-split conduction-band and M-shaped valence-band states. Furthermore, for large charge transfer, we found a new topological Dirac cone at the top surface, originating from the Rashba-split conduction-band states that moved downwards. This result suggests possible reinterpretations of experiments because this new Dirac cone might have been observed by ARPES measurements instead of the original one.

One caveat of our DFT calculations is that we considered periodic arrangements of K adatoms, while periodicity in K adatoms may be difficult to achieve experimentally. However, major qualitative features of our study still remain relevant to thin TI slabs with different types of adsorption layers. A good agreement between the DFT and the tight-binding calculations, supports the validity of our approach. The key elements in engineering surface states of TIs with asymmetric surfaces, are the amount of charge transfer at the adsorbed surface, the hybridization between the top and bottom surface, and the bulk band gap value.

References

[1] Fu L and Kane C L 2007 Topological insulators with inversion symmetry *Phys. Rev.* B **76** 045302
[2] Teo J C, Fu L and Kane C L 2008 Surface states and topological invariants in three-dimensional topological insulators: application to $Bi_{1−x}Sb_x$ *Phys. Rev.* B **78** 045426
[3] Qi X L, Hughes T L and Zhang S C 2008 Topological field theory of time-reversal invariant insulators *Phys. Rev.* B **78** 195424
[4] Hasan M Z and Kane C L 2010 Colloquium: topological insulators *Rev. Mod. Phys.* **82** 3045–67
[5] Qi X and Zhang S C 2011 Topological insulators and superconductors *Rev. Mod. Phys.* **83** 1057–110
[6] Fu L and Kane C L 2008 Superconducting proximity effect and Majorana fermions at the surface of a topological insulator *Phys. Rev. Lett.* **100** 096407
[7] Yu R, Zhang W, Zhang H J, Zhang S C, Dai X and Fang Z 2010 Quantized anomalous Hall effect in magnetic topological insulators *Science* **329** 61–4
[8] Chang C-Z *et al* 2013 Experimental observation of the quantum anomalous Hall effect in a magnetic topological insulator *Science* **340** 167–70
[9] Hsieh D *et al* 2009 Observation of unconventional quantum spin textures in topological insulators *Science* **323** 919–22
[10] Zhang H, Liu C X, Qi X L, Dai X, Fang Z and Zhang S C 2009 Topological insulators in Bi_2Se_3, Bi_2Te_3 and Sb_2Te_3 with a single Dirac cone on the surface *Nature Phys.* **5** 438–42
[11] Noh H-J *et al* 2008 Spin–orbit interaction effect in the electronic structure of Bi_2Te_3 observed by angle-resolved photoemission spectroscopy *Europhys. Lett.* **81** 57006
[12] Hsieh D *et al* 2009 A tunable topological insulator in the spin helical Dirac transport regime *Nature* **460** 1101–5

[13] Park S R, Jung W S, Kim C, Song D J, Kim C, Kimura S, Lee K D and Hur N 2010 Quasiparticle scattering and the protected nature of the topological states in a parent topological insulator Bi_2Se_3 *Phys. Rev.* B **81** 041405

[14] Analytis J G, Chu J-H, Chen Y, Corredor F, McDonald R D, Shen Z X and Fisher I R 2010 Bulk Fermi surface coexistence with Dirac surface state in Bi_2Se_3: a comparison of photoemission and Shubnikov de Haas measurements *Phys. Rev.* B **81** 205407

[15] Bianchi M, Guan D, Bao S, Mi J, Iversen B B, King P D C and Hofmann P 2010 Coexistence of the topological state and a two-dimensional electron gas on the surface of Bi_2Se_3 *Nature Commun.* **1** 128

[16] King P D C *et al* 2011 Large tunable Rashba spin splitting of a two-dimensional electron gas in Bi_2Se_3 *Phys. Rev. Lett.* **107** 096802

[17] Bianchi M, Hatch R C, Mi J, Iversen B B and Hofmann P 2011 Simultaneous quantization of bulk conduction and valence states through adsorption of nonmagnetic impurities on Bi_2Se_3 *Phys. Rev. Lett.* **107** 086802

[18] Benia H M, Lin C, Kern J and Ast C R 2011 Reactive chemical doping of the Bi_2Se_3 topological insulator *Phys. Rev. Lett.* **107** 177602

[19] Zhu Z H *et al* 2011 Rashba spin-splitting control at the surface of the topological insulator Bi_2Se_3 *Phys. Rev. Lett.* **107** 186405

[20] Chen C *et al* 2012 Robustness of topological order and formation of quantum well states in topological insulators exposed to ambient environment *Proc. Natl Acad. Sci. USA* **109** 3694–8

[21] Bahramy M S *et al* 2012 Emergent quantum confinement at topological insulator surfaces *Nature Commun.* **3** 1159

[22] Bianchi M, Hatch R C, Guan D, Planke T, Mi J, Iversen B B and Hofmann P 2012 The electronic structure of clean and adsorbate-covered Bi_2Se_3: an angle-resolved photoemission study *Semicond. Sci. Technol.* **27** 124001

[23] He X, Zhou W, Wang Z Y, Zhang Y N, Shi J, Wu R Q and Yarmoff J A 2013 Surface termination of cleaved Bi_2Se_3 investigated by low energy ion scattering *Phys. Rev. Lett.* **110** 156101

[24] Urazdin S, Bilc B, Mahanti S D, Tessmer S H, Kyratsi T and Kanatzidis M G 2004 Surface effects in layered semiconductors Bi_2Se_3 and Bi_2Te_3 *Phys. Rev.* B **69** 085313

[25] Menshchikova T V, Eremeev S V and Chulkov E V 2012 On the origin of two-dimensional electron gas states at the surface of topological insulators *JETP Lett.* **92** 106–11

[26] Kresse G and Furthmüller J 1996 Efficient iterative schemes for *ab initio* total-energy calculations using a plane-wave basis set *Phys. Rev.* B **54** 11169–86

[27] Kresse G and Furthmülle J 1996 Efficiency of *ab initio* total energy calculations for metals and semiconductors using a plane-wave basis set *Comput. Mater. Sci.* **6** 15–50

[28] Blöchl P E 1994 Projector augmented-wave method *Phys. Rev.* B **50** 17953–79

[29] Perdew J P, Burke K and Ernzerhof M 1996 Generalized gradient approximation made simple *Phys. Rev. Lett.* **77** 3865–8

[30] Lovett D R 1977 *Semimetals and Narrow-Bandgap Semiconductors* 1st edn (London: Pion Limited)

[31] Nakajima S 1963 The crystal structure of $Bi_2Te_{3-x}Se_x$ *J. Phys. Chem. Solids* **24** 479–85

[32] Kobayashi K 2011 Electron transmission through atomic steps of Bi_2Se_3 and Bi_2Te_3 surfaces *Phys. Rev.* B **84** 205424

[33] Slater J C and Koster G F 1954 Simplified LCAO method for the periodic potential problem *Phys. Rev.* **94** 1498–524

[34] Park K, Heremans J J, Scarola V W and Minic D 2010 Robustness of topologically protected surface states in layering of Bi_2Te_3 thin films *Phys. Rev. Lett.* **105** 186801

[35] Jin H, Song J H and Freeman A 2011 Dirac cone engineering in Bi_2Se_3 thin films *Phys. Rev.* B **83** 125319

[36] Shan W Y, Lu H Z and Shen S Q 2010 Effective continuous model for surface states and thin films of three-dimensional topological insulators *New J. Phys.* **12** 043048